

Multidimensional Local Binary Pattern for Hyperspectral Image Classification

Yanshan Li^{ID}, Haojin Tang^{ID}, Weixin Xie, and Wenhan Luo^{ID}

Abstract—For the large amount of spatial and spectral information contained in hyperspectral image (HSI), feature description of HSI has attracted widespread concern in recent years. Existing deep learning-based HSI feature description algorithms require a large number of training samples and have poor interpretability. Therefore, it is necessary to develop an efficient HSI features description algorithm with interpretability based on machine learning. Local binary pattern (LBP) is a classical descriptor used to extract the local spatial texture features of images, which has been widely applied to image feature description and matching. However, the existing LBP algorithms for HSI are based on the single-dimensional description, which leads to the limitations on the expression of spatial-spectral information. Therefore, a multidimensional LBP (MDLBP) based on Clifford algebra for HSI is proposed in this article, which is able to extract spatial-spectral feature from multiple dimensions. First, with the theory of the Clifford algebra, a new representation of HSI including spatial and spectral information is built. Second, the geometric relationship between the local geometry of HSI in Clifford algebra space is calculated to realize the local multidimensional description of the local spatial-spectral information. Finally, a novel LBP coding algorithm for HSI is implemented based on the local multidimensional description to calculate the feature descriptor of HSI. The experimental results on HSI classification show that our proposed MDLBP algorithm can achieve higher accuracy than the representative spatial-spectral features and the existing LBP algorithms, especially in the scenery of small-scale training samples.

Index Terms—Clifford algebra, hyperspectral image (HSI), local binary pattern (LBP), machine learning, multidimensional description.

I. INTRODUCTION

HYPERSPECTRAL image (HSI) contains not only the spatial feature of the object but also the spectral information of the object. In recent years, HSI is widely applied to

Manuscript received October 13, 2020; revised March 2, 2021; accepted March 18, 2021. This work was supported in part by the National Natural Science Foundation of China under Grant 61771319 and Grant 61871154, in part by the Natural Science Foundation of Guangdong Province under Grant 2017A030313343 and Grant 2019A1515011307, in part by the Shenzhen Science and Technology Project under Grant JCYJ20180507182259896, and in part by the Other Project under Grant WDZC20195500201. (*Corresponding authors:* Yanshan Li; Haojin Tang.)

Yanshan Li, Haojin Tang, and Weixin Xie are with the ATR National Key Laboratory of Defense Technology, Shenzhen University, Shenzhen 518060, China, and also with the Guangdong Key Laboratory of Intelligent Information Processing, Shenzhen University, Shenzhen 518060, China (e-mail: lys@szu.edu.cn; tanghaojin2018@email.szu.edu.cn).

Wenhan Luo is with Tencent, Shenzhen 518057, China (e-mail: whluo.china@gmail.com).

Color versions of one or more figures in this article are available at <https://doi.org/10.1109/TGRS.2021.3069505>.

Digital Object Identifier 10.1109/TGRS.2021.3069505

various fields, such as biomedicine [1], [2], agriculture [3], [4], mineralogy [5], [6], military [7], and face recognition [8], [9]. Since the feature extracted from HSI is the basic of these applications, how to efficiently extract and describe the features of HSI has become a research hot spot.

The existing deep learning-based HSI feature description algorithms typically require a large number of labeled samples in the training process. However, due to the complex shooting environment of HSI, it is difficult to obtain sufficient labeled samples for the deep learning-based algorithms. In addition, since the deep neural network is usually regarded as a “black box,” the deep learning-based description algorithms of HSI are unexplainable, which limits its application for military, biomedical, and other fields.

Local binary pattern (LBP) [10] is a local feature description algorithm, which has the advantage of creative theory and low computational complexity. Moreover, it can provide the rotation invariance and understandability. LBP is widely used in various fields, such as texture analysis of gray-scale images [11], spatio-temporal feature description of video sequence frames [12], detection and tracking of pedestrians and vehicle targets [13], biological and medical image analysis [14], and 3-D image feature description [15]. LBP has also been successfully applied to HSI, such as HSI matching and classification [16]–[18].

However, HSI exhibits the characteristics of strong correlation between bands and additional spectral information. Most of the existing LBP algorithms for HSI are the extension versions of the LBP designed for gray image, which describes only the spatial-spectral features of HSI in a single dimension, and does not consider the characteristics of high-dimensional data in spatial-spectral domain. Therefore, based on the Clifford algebra, a multidimensional LBP (MDLBP) is proposed to fully describe the spatial-spectral information from multiple dimensions. Specifically, the contribution of this article mainly includes the following four aspects.

- 1) A local multidimensional description model (LMDM) in Clifford algebra space is proposed as the basis of HSI processing. It calculates the geometric relationship from multiple dimensions to obtain a local multidimensional description set, which can effectively represent the local spatial-spectral information.
- 2) Based on LMDM, an effective LBP coding method is designed for HSI classification. It can learn the discriminative MDLBP features by analyzing the geometric difference of HSI pixels in a local neighborhood.

- 3) It provides a novel extensible framework to learn spatial-spectral feature in Clifford algebra space. More importantly, it gives a mathematical explanation for the combination of spatial and spectral features.
- 4) Due to the multidimensional geometric analysis, our proposed MDLBP algorithm achieves better performance than the spatial-spectral features and the existing LBP algorithms, especially when the number of training samples is small.

II. RELATE WORK

A. Local Binary Pattern

In 2002, Ojala *et al.* [10] proposed the original LBP which is defined in the 3×3 square neighborhood for the gray-scale image. In order to achieve the gray-scale invariance, the gray value of the central pixel is considered as the threshold in the square neighborhood and is compared with the gray values of its adjacent neighboring pixels. If the gray values of the neighboring pixels are greater than that of the central pixel, the location of it in the neighborhood will be marked as 1, otherwise 0. It can be formulated as follows:

$$s(g_p - g_c) = \begin{cases} 1, & g_p - g_c \geq 0 \\ 0, & g_p - g_c < 0 \end{cases} \quad (p = 0, \dots, P) \quad (1)$$

where g_p is the gray value of the neighboring pixels, g_c is the gray value of the central pixels, and P is the number of neighboring pixels. However, the original LBP descriptor is limited in a fixed region, which cannot adapt to texture features of different scales. For this reason, Ojala *et al.* [10] improved the LBP descriptor by expanding the square neighborhood to the circular neighborhood with radius R . To achieve the rotation invariance, they continuously rotate the circular neighborhood of the central pixel, and obtain a series of different LBP values, taking the minimum value as the final LBP value of the circular neighborhood. As the extension of LBP, volume LBP (VLBP) and LPBs from three orthogonal planes (LBP-TOP) descriptor proposed by Zhao *et al.* [19] can fully represent the temporal information of dynamic texture, and effectively reduce the computational complexity.

In recent years, LBP algorithm has been applied to feature extraction of HSI [16]–[18], [20]–[26]. Song *et al.* [16] applied LBP to the description of rotation-invariant texture features of remote sensing images, and achieved better classification results than spectral features. Due to the important role of spatial information on HSI, a complete LBP (CLBP) which is suitable for multiple scenes is proposed to describe the spatial feature of HSI. Li *et al.* [17] combined the two-dimensional uniform LBP (2-D-ULBP) with an extreme learning machine (ELM) to construct an effective HSI classification framework, which shows excellent performance on several HSI data sets. Ye *et al.* [21] proposed a sign-and-magnitude LBP algorithm for HSI classification, and utilized Markov random field as a prior probability to calculate the Bayesian maximum of HSI classification. Jia *et al.* [18] proposed a 3-D LBP descriptor based on the octahedron structure, which can describes the joint distribution of spatial-spectral features of HSI. Besides, convolutional neural network (CNN) combined with LBP algorithms for HSI classification [25], [26] has also been

proposed, which aims to use the LBP algorithm to reduce the computational cost of CNN.

The above LBP algorithm and its extended algorithms are limited to a single dimension when describing the spatial-spectral feature, ignoring the characteristics of high-dimensional data in the spatial-spectral domain. Therefore, it has become an urgent need to develop an algorithm that can fully describe and extract the spatial-spectral information of HSI from multiple dimensions.

B. Spatial-Spectral Feature for HSI

Feature extraction is the basis of HSI processing and application. Since HSI contains both spatial and spectral information of the object, how to efficiently extract the spatial-spectral feature has attracted widespread attention in recent years. To tackle the HSI classification task, a variety of spatial-spectral features extraction algorithms have been proposed, which can be divided into two types, as follows.

The former type is the handcraft feature-based algorithms [27]–[32]. It utilizes the 3-D descriptors to directly extract joint spatial-spectral features. Cao *et al.* [27] designed a 3-D discrete wavelet transform (3-D-DWT) texture feature to describe the spatial-spectral information of HSI effectively. Lin *et al.* [28] proposed a 3-D Gabor-based approach for pixel-based HSI classification, which improves the classification accuracy substantially. Scovanner and Paul [29], Li and Shi [30], and Li *et al.* [31] applied the 3-D scale-invariant feature transform (3-D-SIFT) to the HSI classification, and developed a more robust SIFT descriptor, namely, the tensor gradient SIFT (TGSIFT) descriptor for spatial-spectral feature extraction. In addition, an extended multiattribute profile (EMAP) [32] algorithm was proposed to exploit the spatial-spectral feature which provides excellent classification results for different HSI data sets. However, this kind of algorithm describes the spatial-spectral features directly without analyzing the HSI structure. In other words, it lacks an effective mathematical model, which can provide a unified interpretation for the combination of spatial and spectral features.

The latter type is the deep learning-based algorithms [33]–[36]. It mainly adopts the CNN to learn effective spatial-spectral features. Li *et al.* [33] proposed a 3-D-CNN framework for accurate HSI classification without relying on any preprocessing or postprocessing. Hamida *et al.* [34] explored the performance of DL architectures for the HSI classification and designed a 3-D deep learning approach that enables a joint spatial and spectral information process. To avoid overfitting in data modeling, Chen *et al.* [35] presented a 3-D CNN-based feature extraction method with combined regularization to extract effective spatial-spectral features of HSI. He *et al.* [36] proposed a novel multiscale 3-D CNN-based algorithm, which can jointly learn both 2-D multiscale spatial feature and 1-D spectral feature from HSI. Although such kind of algorithms can achieve state-of-the-art performance with sufficient training samples, its classification performance will degrade dramatically in a small training sample case. Meanwhile, deep learning-based algorithms lack the explanation for its decision making.

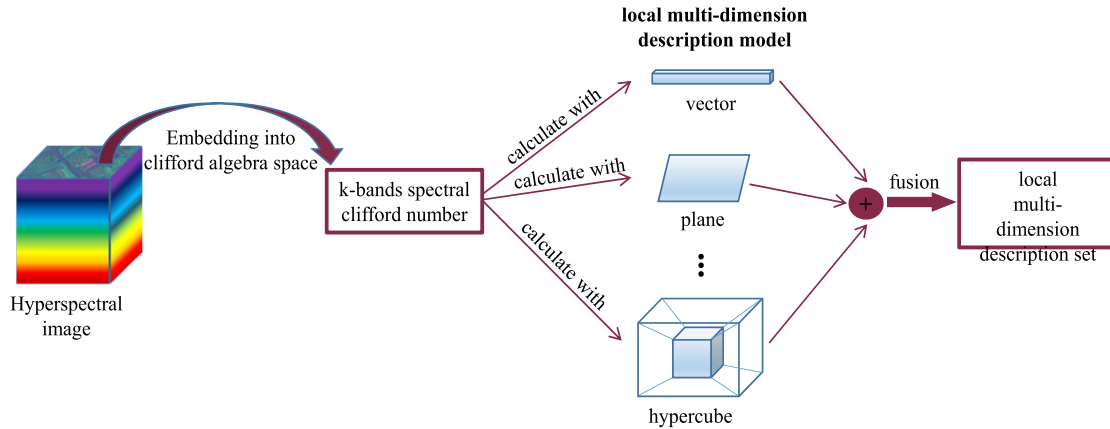


Fig. 1. Local multidimensional description model for HSI in the Clifford algebra space.

In summary, due to the higher requirement for both military and medical treatment, it is reasonable for us to develop a spatial–spectral feature extraction algorithm which can provide strict mathematical explanation and achieve excellent performance in the scenery of small-scale training samples.

C. Clifford Algebra Model for HSI

Clifford algebra [37]–[42] is a mathematical tool based on dimension operation. It provides an effective framework to perform the calculation without using the coordinate information, which can improve the calculation efficiency and reduce the calculation complexity. This algebraic method is based on inner product as well as outer product. It constructs the expression of geometry in a coordinate-free way, which unifies the calculation of multidimensional geometry. At present, Clifford algebra has been widely used in physics [43], sensor network [44], computer vision [45]–[47], and other fields.

In multidimensional Clifford algebra space, it provides us with a variety of geometric operation methods, such as inner product, outer product, geometric product, projection, and angle. These methods are mainly used to implement the geometric analysis in the multidimensional space, such as spatial structure construction and spatial transformation, geometric measurement and geometric relationship calculation, feature extraction, and motion expression.

Let $f(x, y)$ be the HSI. According to [48], it can be expressed in the Clifford algebra space as follows:

$$f(x, y) = \sum_{i=1}^n f_i(x, y) e_i \quad (2)$$

where $f_i(x, y)$ is the i th band image of $f(x, y)$, (x, y) denotes the spatial coordinate, and n is the number of bands. Then, the 3-D spatial–spectral domain of HSI can be expressed as \mathcal{G}_n in the Clifford algebra space, and e_1, e_2, \dots, e_n is the orthogonal basis of \mathcal{G}_n .

For vectors \mathbf{x} and \mathbf{y} , their geometric product \mathbf{xy} is defined as follows:

$$\mathbf{xy} = \mathbf{x} \cdot \mathbf{y} + \mathbf{x} \wedge \mathbf{y} \quad (3)$$

where $\mathbf{x} \cdot \mathbf{y}$ is the inner product and $\mathbf{x} \wedge \mathbf{y}$ is the outer product. It is a mixed-dimensional object which contains both the scalar part $\mathbf{x} \cdot \mathbf{y}$ and the vector part $\mathbf{x} \wedge \mathbf{y}$.

Assuming that $b_1, b_2, \dots, b_k \in \mathcal{G}_n$ is linearly independent, the k -patch in the Clifford algebra space of HSI can be represented as follows:

$$B_k = \langle b_1 b_2, \dots, b_k \rangle_k = b_1 \wedge b_2, \dots, \wedge b_k \quad (4)$$

where B_k is the k -patch. Therefore, with respect to the n' -dimensional subspace $\mathcal{G}_{n'}$ of \mathcal{G}_n , there is always a n' -patch which makes $\mathcal{G}_{n'}$ be constructed with solution set x of $x \wedge B_{n'} = 0, x \in \mathcal{G}_{n'}$. Therefore, the subspace $\mathcal{G}_{n'}$ can be uniquely determined by the unitized patch $B_{n'}$. According to Cramer's theorem, starting from a basis $b_1, b_2, \dots, b_{n'}$, an orthogonal basis $e_1, e_2, \dots, e_{n'}$ which constitutes the subspace $\mathcal{G}_{n'}$ can be obtained. For any vector $b \in \mathcal{G}_{n'}$, it can be expanded as follows:

$$b = \sum_{i=1}^{n'} \alpha_i e_i \quad (5)$$

where α_i is the component of the vector b regarding orthogonal basis $e_1, e_2, \dots, e_{n'}$.

III. LOCAL MULTIDIMENSIONAL DESCRIPTION MODEL FOR HSI IN CLIFFORD ALGEBRA SPACE

To fully combine the spatial and spectral feature information of HSI, a local multidimensional description model under \mathcal{G}_n space for HSI is proposed in this article. In \mathcal{G}_n space, the geometric relationship between the local geometry of HSI is calculated from different dimensions by using a variety of geometric operations provided by Clifford algebra, so as to realize the effective description of the local spatial–spectral information. Fig. 1 shows the schematic of the LMDM for HSI in the Clifford algebra space.

Assuming that $f_\lambda(x, y)$ is the spectral response of the λ th band of $f(x, y)$ with spatial coordinate (x, y) , to obtain the local geometric expression of $f_\lambda(x, y)$ in \mathcal{G}_n space, $k/$ -bands spectral Clifford number (KB-SCN) of $f_\lambda(x, y)$ is defined

based on (2), as follows:

$$f'_\lambda(x, y) = \sum_{i=1}^k f'_{\lambda+i-1}(x, y) e_{\lambda+i-1} \quad (6)$$

where $f'_\lambda(x, y)$ represents the KB-SCN.

In order to further extract the local spatial-spectral information of HSI, we implement the local multidimensional description for $f'_\lambda(x, y)$. Thus the local multidimensional description set $\psi(f'_\lambda(x, y))$ of $f'_\lambda(x, y)$ can be expressed as follows:

$$\psi(f'_\lambda(x, y)) = \{\kappa_1(f'_\lambda(x, y), S_1), \dots, \kappa_i(f'_\lambda(x, y), S_i), \dots, \kappa_m(f'_\lambda(x, y), S_m)\} \quad (7)$$

where $S_i \in \mathcal{G}_n$ denotes the local reference geometry which is used for the local geometric relationship calculation of HSI, $\kappa_i(f'_\lambda(x, y), S_i)$ represents the geometric relationship between $f'_\lambda(x, y)$, and S_i , m denotes the number of descriptors in a local multidimensional description set. Based on the dimension of local geometry S_i , we discuss the type of $\kappa_i(f'_\lambda(x, y), S_i)$ in this article as follows.

1-D Local Description: When S_i is a vector, 1-D local description for spatial-spectral feature of HSI is implemented by using geometric operations such as length and angle of basic vector.

Let $S_1 = f'_\lambda(x, y)$, the 1-D descriptor in the local multidimensional description set of $f'_\lambda(x, y)$ can be expressed as follows:

$$\kappa_1(f'_\lambda(x, y), S_1) = \|f'_\lambda(x, y)\| = f'_\lambda(x, y) \cdot f'_\lambda(x, y) \quad (8)$$

where $\kappa_1(f'_\lambda(x, y), S_1)$ is the length of $f'_\lambda(x, y)$. In the subsequent MDLBP coding, $\kappa_1(f'_\lambda(x, y), S_1)$ essentially represents the difference between the joint spectral values distribution of k adjacent pixels corresponding to different spectral curves, which effectively describes the local spatial-spectral information of HSI.

Furthermore, in order to obtain the vector which can calculate the local geometric relationship more effectively, central basic vector I_k is defined in the k -dimensional Clifford algebra space, as follows:

$$I_k = \frac{1}{k} \sum_{i=1}^k e_i \quad (9)$$

where I_k denotes the sum of orthogonal basis in k -dimensional Clifford algebra space, and $e_i (i = 1, \dots, k)$ is the orthogonal basis of k -dimensional Clifford algebra space. Let $S_2 = I_k$, thus the 1-D descriptor in the local multidimensional description set can also be expressed as follows:

$$\kappa_2(f'_\lambda(x, y), S_2) = \frac{f'_\lambda(x, y) \cdot I_k}{\|f'_\lambda(x, y)\| \|I_k\|} \quad (10)$$

where $\kappa_2(f'_\lambda(x, y), S_2)$ is the cosine value between $f'_\lambda(x, y)$ and I_k .

As Fig. 2 shows, let $k = 3$, we thus have $I_3 = (e_1 + e_2 + e_3)/3$. Besides, the three axes $\lambda_1, \lambda_2, \lambda_3$ represent the spectral response values of three adjacent bands. By calculating the cosine value between three-bands spectral Clifford numbers (3B-SCNs) and I_3 , the 1-D local description of

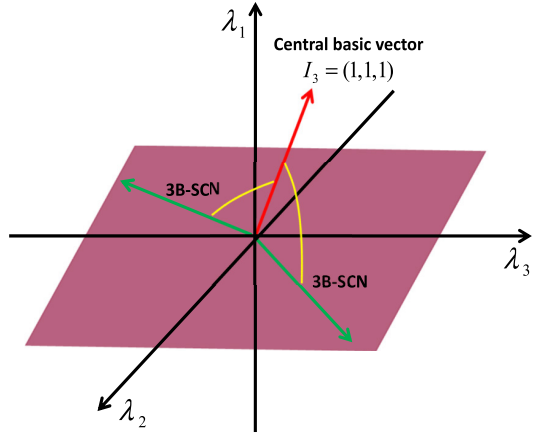


Fig. 2. Geometry relationship calculation between 3B-SCN and center basic vector in the 3-D Clifford algebra space of HSI.

$f'_\lambda(x, y)$ is achieved. When k increases or decreases, it can also calculate the 1-D local description of $f'_\lambda(x, y)$ based on the above method. In the subsequent MDLBP coding, $\kappa_2(f'_\lambda(x, y), S_2)$ can be considered as the difference between the joint gradient distribution of k adjacent pixels corresponding to different spectral curves, which aims to describe the local spatial-spectral information of HSI based on the speed of gradient change.

2-D Local Description: When S_i is a plane, 2-D local description for spatial-spectral feature of HSI is carried out by using geometric operations such as the angle of plane and the plane projection.

Let β be a 2-D plane. It can be represented by the outer product of two basis vectors in the Clifford algebra space, as follows:

$$\beta = e_j \wedge e_k \quad (11)$$

where e_j and e_k are the orthogonal basis of σ_n . By calculating the cosine value between $f'_\lambda(x, y)$ and β , the local spatial-spectral information of HSI can be described effectively.

Writing $S_3 = \beta$, the 2-D descriptor in the local multidimensional description set of $f'_\lambda(x, y)$ can be expressed as follows:

$$\kappa_3(f'_\lambda(x, y), S_3) = \cos\left(90^\circ - \arccos\left(\frac{f'_\lambda(x, y) \cdot W}{\|f'_\lambda(x, y)\| \|W\|}\right)\right) \quad (12)$$

where $\kappa_3(f'_\lambda(x, y), S_3)$ is the cosine value between $f'_\lambda(x, y)$ and β , and W is the normal vector of β .

To further reduce the calculation complexity between $f'_\lambda(x, y)$ and β , the calculation of cosine value between $f'_\lambda(x, y)$ and β can be transformed into the calculation of the projection of $f'_\lambda(x, y)$ on β . Similarly, let $S_4 = \beta$, the 2-D descriptor in the local multidimensional description set of $f'_\lambda(x, y)$ can be also expressed as follows:

$$\kappa_4(f'_\lambda(x, y), S_4) = \frac{f'_\lambda(x, y) \cdot W}{\|W\|} \quad (13)$$

where $\kappa_4(f'_\lambda(x, y), S_4)$ denotes the projection of $f'_\lambda(x, y)$ on β , and W is the normal vector of β . In the subsequent MDLBP

coding, $\kappa_4(f'_\lambda(x, y), S_4)$ can be considered as the difference between the joint peak values distribution of k adjacent pixels corresponding to different spectral curves, which aims to describe the local spatial-spectral information of HSI based on the change of local peak values.

n-Dimensional Local Description: More generally, when S_i is the n -dimensional geometry, n -dimensional local description for spatial-spectral feature of HSI is implemented by using the cosine value between $f'_\lambda(x, y)$ and n -dimensional geometry.

Let σ_n be the n -dimensional geometry. It can be represented by the outer product of n basic vectors in the Clifford algebra space, as follows:

$$\sigma_n = e_1 \wedge e_2 \wedge e_3 \wedge e_4, \dots, e_n \quad (14)$$

where e_1, e_2, \dots, e_n are the orthonormal basis of σ_n .

Let $S_i = \sigma_n$, thus the n -dimensional descriptor in the local multidimensional description set of $f'_\lambda(x, y)$ can be considered as the cosine value between $f'_\lambda(x, y)$ and σ_n , as follows:

$$\kappa_i(f'_\lambda(x, y), S_i) = \frac{f'_\lambda(x, y) \cdot \sigma_n}{\|f'_\lambda(x, y)\| \|\sigma_n\|} \quad (15)$$

where $\kappa_i(f'_\lambda(x, y), S_i)$ is the cosine value between $f'_\lambda(x, y)$ and σ_n , $n \geq 2$.

Similarly, in order to further reduce the calculation complexity between $f'_\lambda(x, y)$ and σ_n , the calculation of the cosine value between $f'_\lambda(x, y)$ and σ_n can be transformed into the calculation of the projection of $f'_\lambda(x, y)$ on σ_n . Let $f'_\lambda(x, y)^\parallel$ be the parallel component of $f'_\lambda(x, y)$ relative to σ_n , and $f'_\lambda(x, y)^\perp$ be the vertical component of $f'_\lambda(x, y)$ relative to σ_n . They satisfy the following equations:

$$f'_\lambda(x, y)^\parallel + f'_\lambda(x, y)^\perp = f'_\lambda(x, y) \quad (16)$$

$$f'_\lambda(x, y)^\parallel \wedge \sigma_n = 0 \quad (17)$$

$$f'_\lambda(x, y)^\perp \cdot \sigma_n = 0. \quad (18)$$

By calculating the geometric product of $f'_\lambda(x, y)^\perp$ and σ_n , the projection of $f'_\lambda(x, y)$ on σ_n can be expressed as follows:

$$\begin{aligned} f'_\lambda(x, y)^\perp \cdot \sigma_n &= f'_\lambda(x, y)^\perp \cdot \sigma_n + f'_\lambda(x, y)^\perp \wedge \sigma_n \\ &= f'_\lambda(x, y)^\perp \wedge \sigma_n \\ &= f'_\lambda(x, y)^\perp \wedge \sigma_n + f'_\lambda(x, y)^\parallel \wedge \sigma_n \\ &= f'_\lambda(x, y) \wedge \sigma_n \end{aligned} \quad (19)$$

where $f'_\lambda(x, y)^\perp$ can be regarded as the projection of $f'_\lambda(x, y)$ on σ_n . Similarly, let $S_i = \sigma_n$, both sides of (19) are divided by σ_n , thus another expression of n -dimensional descriptors in the local multidimensional description set of $f'_\lambda(x, y)$ can be obtained as follows:

$$\kappa_i(f'_\lambda(x, y), S_i) = \frac{f'_\lambda(x, y) \wedge \sigma_n}{\sigma_n} \quad (20)$$

where $\kappa_i(f'_\lambda(x, y), S_i)$ represents the projection of $f'_\lambda(x, y)$ on σ_n .

To sum up, based on the expression of HSI in the Clifford algebra space, the geometric relationship between the local geometry of HSI is calculated from vector, plane, hypergeometry, and other dimensions. Besides, the local multidimensional description set which can fully represent the local spatial-spectral feature of HSI is obtained, and the fusion

methods for elements of the multidimensional description set, such as concatenation and weighted average, can be designed according to the needs of researchers. In our experiment, all elements of the multidimensional description set are fused by concatenation. Moreover, it provides a more robust and explainable feature description model for the subsequent efficient local coding.

IV. MULTIDIMENSIONAL LOCAL BINARY PATTERN FOR HSI

Based on the LMDM of HSI, the local spatial-spectral information is fully and effectively extracted. In order to realize the local binary coding of spatial-spectral information of HSI, we combine the original LBP to propose a novel MDLBP for HSI.

Assuming that $f_\lambda(x_c, y_c)$ is the spectral response values of the HSI pixels with spatial coordinate (x_c, y_c) at λ bands, according to (6), the KB-SCN of $f_\lambda(x_c, y_c)$ can be expressed as follows:

$$f'_\lambda(x_c, y_c) = \sum_{i=1}^k f_{\lambda+i-1}(x_c, y_c) e_{\lambda+i-1} \quad (21)$$

where $f'_\lambda(x_c, y_c)$ represents the KB-SCN of $f_\lambda(x_c, y_c)$.

According to the LBP for gray image, neighborhood information U is defined as the joint contribution of P ($P > 1$) KB-SCNs centered on $f'_\lambda(x_c, y_c)$ ($f'_{\lambda,c}$ for shot), as follows:

$$U = u(f'_{\lambda,c}, f'_{\lambda,0}, \dots, f'_{\lambda,P-1}) \quad (22)$$

where $f'_{\lambda,0}, \dots, f'_{\lambda,P-1}$ represent the KB-SCNs which are uniformly distributed in the circle symmetric neighborhood with the radius R ($R > 0$) centered on $f'_{\lambda,c}$. Because the spatial coordinate of $f'_{\lambda,c}$ in the spatial domain is (x_c, y_c) , thus the spatial coordinate of f'_p ($0 \leq p \leq P-1$) can be calculated as $(x_c + R \cos(2\pi p/P), y_c - R \sin(2\pi p/P))$ for the sampling points which do not completely fall in the center of HSI pixel, their KB-SCNs will be calculated by bilinear quadratic interpolation.

From Section III, we know that the LMDM of HSI is extensible. In this article, we mainly explore the LMDM based on the length, the angle of center basis, and the plane projection, and find out its influence on the local binary coding efficiency of KB-SCN. Therefore, let $\psi'(f'_\lambda(x, y))$ be the local multidimensional description set based on the fusion of the length, the angle of center basis, and the plane projection, according to (8), (10), and (12), it can be expressed as follows:

$$\begin{aligned} \psi'(f'_\lambda(x, y)) &= \{\kappa_1(f'_\lambda(x, y), S_1), \kappa_2(f'_\lambda(x, y), S_2) \\ &\quad \kappa_3(f'_\lambda(x, y), S_3)\}. \end{aligned} \quad (23)$$

Then, $\psi'(f'_\lambda(x, y))$ is adopted to perform the local multidimensional description for $f'_{\lambda,c}$ and $f'_{\lambda,0}, \dots, f'_{\lambda,P-1}$, as follows:

$$U = u(\psi'(f'_{\lambda,c}), \psi'(f'_{\lambda,0}), \dots, \psi'(f'_{\lambda,P-1})). \quad (24)$$

In order to realize the local multidimensional description invariance of KB-SCN, we first calculate the geometric difference between $\psi'(f'_{\lambda,p})$ ($0 \leq p \leq P-1$) and $\psi'(f'_{\lambda,c})$,

as follows:

$$U = u(\psi'(f'_{\lambda,c}), \psi'(f'_{\lambda,0}) - \psi'(f'_{\lambda,c}), \dots, \psi'(f'_{\lambda,P-1}) - \psi'(f'_{\lambda,c})). \quad (25)$$

The value of $\psi'(f'_{\lambda,p}) - \psi'(f'_{\lambda,c})$ is supposed to be irrelevant to $\psi'(f'_{\lambda,c})$. Thus, (25) is factorized as follows:

$$U \approx u(\psi'(f'_{\lambda,c}))u(\psi'(f'_{\lambda,0}) - \psi'(f'_{\lambda,c}), \dots, \psi'(f'_{\lambda,P-1}) - \psi'(f'_{\lambda,c})). \quad (26)$$

Since the main information of the joint spatial-spectral response distribution is contained in the joint difference distribution, (26) is rewritten as

$$U \approx u(\psi'(f'_{\lambda,0}) - \psi'(f'_{\lambda,c}), \dots, \psi'(f'_{\lambda,P-1}) - \psi'(f'_{\lambda,c})). \quad (27)$$

By considering only the symbol information instead of the numeric values, the local multidimensional description invariance is realized as follows:

$$U \approx u(s(\psi'(f'_{\lambda,0}) - \psi'(f'_{\lambda,c})), \dots, s(\psi'(f'_{\lambda,P-1}) - \psi'(f'_{\lambda,c}))) \quad (28)$$

where $s(x)$ is the same as (1). Finally, let each $\psi'(f'_{\lambda,p}) - \psi'(f'_{\lambda,c})$ be multiplied by binomial coefficient 2^q , then U is transformed into a coding value named $\text{MDLBP}_{P,R}$ which can completely and effectively describe the spatial-spectral feature as follows:

$$\text{MDLBP}_{P,R} = \sum_{q=0}^{P-1} s(\psi'(f'_{\lambda,q}) - \psi'(f'_{\lambda,c})) 2^q. \quad (29)$$

Then, we select the local region of HSI with size $M \times N$ for histogram statistics. The feature vector obtained by statistics is used as the spatial-spectral feature descriptor of the local region, and the bin $h(b)$ of h is expressed as follows:

$$h(b) = \sum_{m=1}^M \sum_{n=1}^N s(\text{MDLBP}_{P,R}(m, n) - b). \quad (30)$$

Finally, based on the traditional LBP descriptor, three orthogonal planes XY , $X\lambda$, and $Y\lambda$ in 3-D spatial-spectral domain are selected to perform the histogram statistics of MDLBP. Then, the MDLBP histograms obtained from the statistics on the three orthogonal planes are connected to finally construct the histogram $h_{XY\lambda}$ which can fully represent the local spatial-spectral information of HSI, as follows:

$$h_{XY\lambda} = [h_{XY}, h_{X\lambda}, h_{Y\lambda}]. \quad (31)$$

The algorithm steps of MDLBP are shown as below.

Step 1: According to (2), the Clifford algebra model for HSI is established, and the corresponding Clifford algebra space named \mathcal{G}_n is built.

Step 2: In \mathcal{G}_n space, the HSI pixels are transformed into the KB-SCN for representation. According to (8), (10), and (12), the length, the angle of central basis vector, and the plane projection are used to perform the multidimensional description for the local spatial-spectral feature of KB-SCN.

Step 3: By calculating the geometric difference between the multidimensional description set of the central KB-SCN

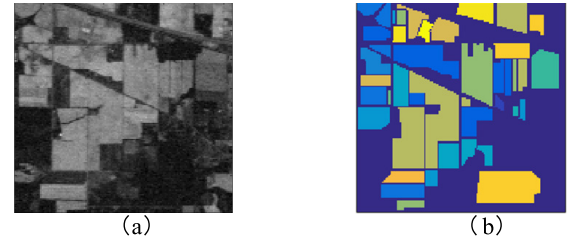


Fig. 3. Indian Pine data set. (a) Ground truth. (b) All sample map.

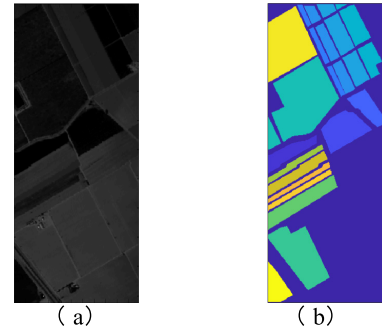


Fig. 4. Salinas scene data set. (a) Ground truth. (b) All sample map.

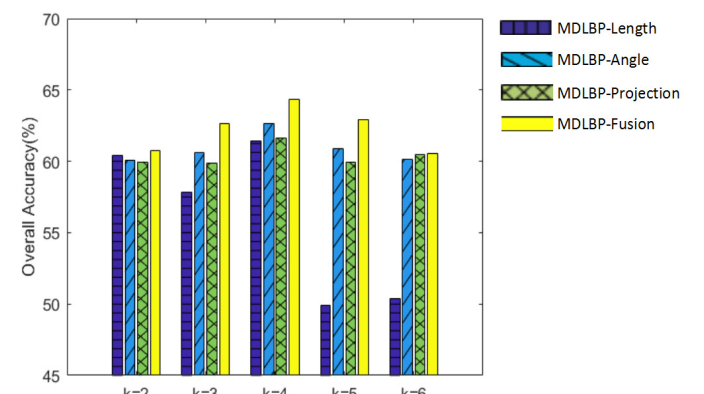


Fig. 5. Parameter tuning of k for the proposed MDLBP descriptor on the Indian Pines data set.

and the neighboring KB-SCN, the local binary coding of the spatial-spectral information in the local neighborhood is implemented, and $\text{MDLBP}_{P,R}$ which can effectively describe the local spatial-spectral feature is obtained.

Step 4: The MDLBP histograms of three orthogonal planes XY , $X\lambda$, and $Y\lambda$ in the 3-D spatial-spectral domain of HSI are obtained by statistics, and the MDLBP histograms of each plane are connected to obtain the $h_{XY\lambda}$ which can completely represent the spatial-spectral feature information of HSI.

V. EXPERIMENTS

In order to verify the effectiveness and accuracy of the MDLBP for the description of spatial-spectral features in the Clifford space, a series of HSI pixel classification experiments are performed on the Indian Pines data set and the Salinas scene data set. In the experiment, MDLBP algorithm is mainly compared with LBP-based algorithms and some representative spatial-spectral feature extraction algorithms.

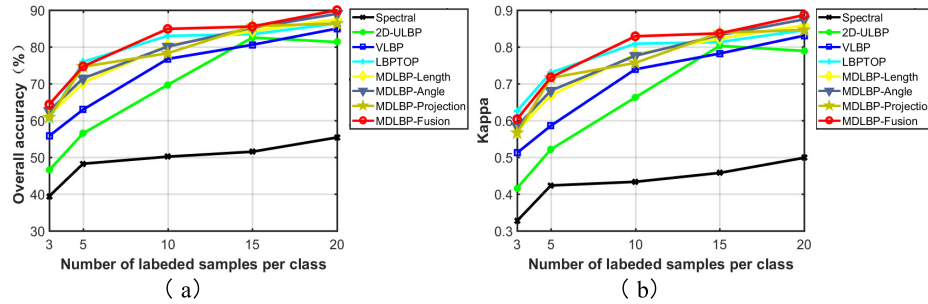


Fig. 6. Influence of training sample size on the Indian Pine data set. (a) OA. (b) Kappa as a function of the number of labeled samples per class.

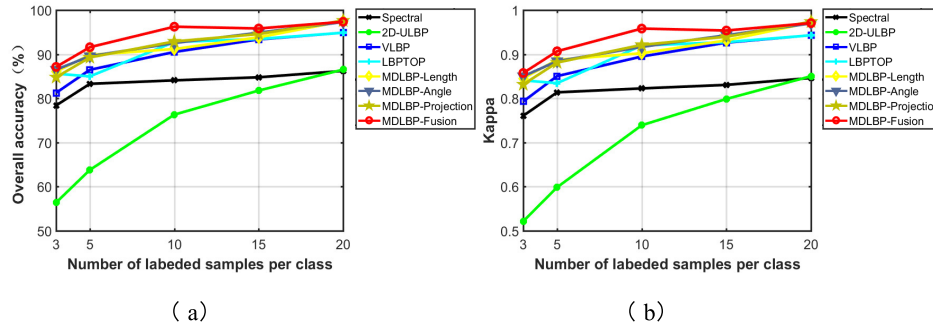


Fig. 7. Influence of training sample size on the Salinas scene data set. (a) OA and (b) Kappa as a function of the number of labeled samples per class.

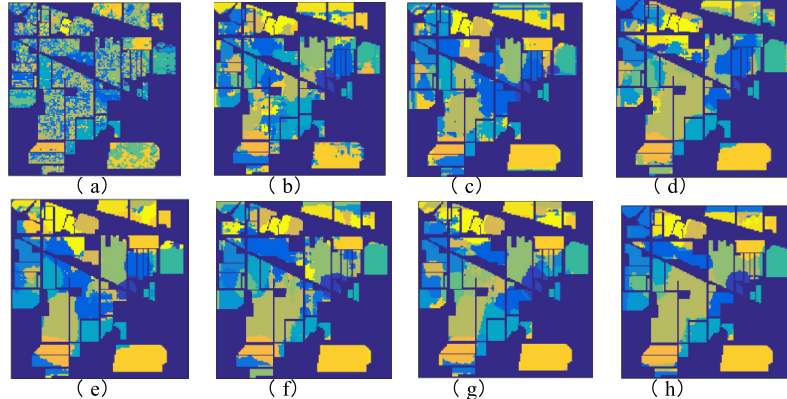


Fig. 8. Indian Pine data set: classification map using (a) spectral, (b) 2-D-ULBP, (c) VLBP, (d) LBP-TOP, (e) MDLBP-length, (f) MDLBP-angle, (g) MDLBP-projection, and (h) MDLBP-fusion.

A. Data Sets

The Indian Pines data set was gathered by AVIRIS sensor in North-western Indiana and it consists of 145×145 pixels with 224 spectral reflectance bands in the wavelength range $(0.4 \sim 2.5) \times 10^{-6}$ m. The data set contains 16 categories of objects, with a total of 10,249 samples. We have also reduced the number of bands to 200 by removing bands covering the region of water absorption. Fig. 3 shows the ground truth and all sample map of the Indian Pines data set.

The Salinas scene data set which contains 16 classes and 54,129 samples was collected by the 224-band AVIRIS sensor over Salinas Valley, California. Its spatial size and resolution are 145×145 pixels and 3.7-m pixels. Fig. 4 shows the ground truth and all sample map of the Salinas scene data set.

B. Experimental Setup

In our experiment, we mainly perform the HSI pixel classification to verify the efficiency and effectiveness of the proposed MDLBP algorithm. Since the HSI contains a lot of redundant information, the HSI data need to be preprocessed before the experiment. Principal component analysis (PCA) [49] is a commonly used algorithm for the data dimensionality reduction. It can reduce the dimensionality by projecting high-dimensional data into a low-dimensional subspace. In this experiment, PCA algorithm is applied for the dimensionality reduction of HSI to extract the representative band data.

After preprocessing, different feature descriptors are used to construct the feature vector of the HSI pixel. In the experiment, our proposed MDLBP algorithm is compared

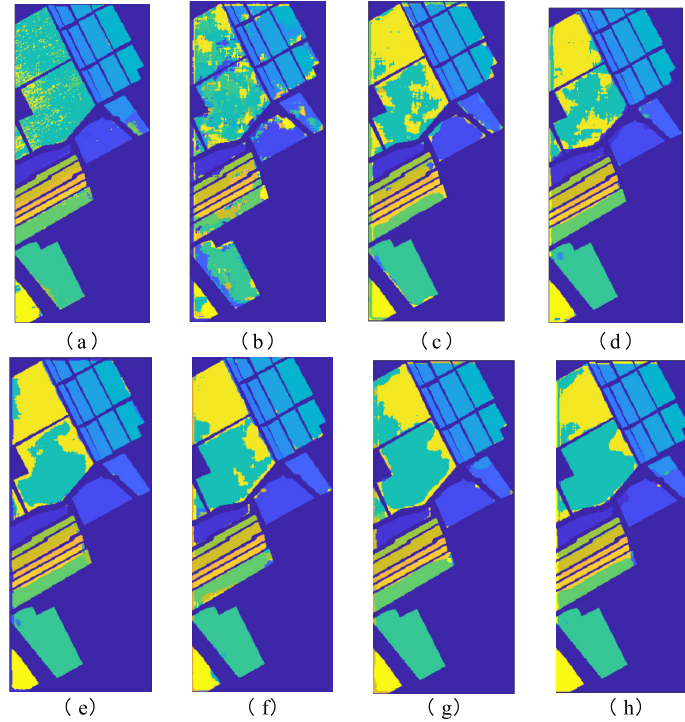


Fig. 9. Salinas scene data set: classification map using (a) spectral, (b) 2-D-ULBP, (c) VLBP, (d) LBP-TOP, (e) MDLBP-length, (f) MDLBP-angle, (g) MDLBP-projection, and (h) MDLBP-fusion.

with 11 representative HSI classification algorithms. More specifically, the original spectral feature is adopted as a baseline, and three LBP-based algorithms are considered, i.e., the 2-D-ULBP, VLBP, and LBP-TOP algorithms. The other seven spatial-spectral feature extraction algorithms are 3-D-DWT [27], 3-D-SIFT [29], 3-D-Gabor [28], TGSIFT [31], 3-D deep learning approach (3-D-DL) [34], 3-D convolutional neural network (3-D-CNN) [33], and multiscale 3-D deep convolutional neural network (M3-D-DCNN) [36]. Since the MDLBP algorithm has characteristics of expansibility and variability, to explore the geometry relationship calculation between local geometry from different dimensions, we first construct three different MDLBP descriptors including MDLBP based on length (MDLBP-length), MDLBP based on the angle of central basis vector (MDLBP-angle), MDLBP based on projection (MDLBP-projection). Then, we fuse the above three MDLBP descriptors to construct the MDLBP based on fusion (MDLBP-Fusion). All the MDLBP descriptors are applied to the experiment for comparison and analysis.

ELM [50] is a novel fast-learning algorithm for solving the single hidden layer neural network. The weights of its output layer are computed using a least squares method and the weights of other layers are randomly assigned, thus the computational cost is much lower than other neural-network-based methods. According to [17], compared to the commonly used standard support vector machine (SVM), which needs to solve a large constrained optimization problem, it has been demonstrated that ELM can provide an HSI classification accuracy that is similar to or even better than that of SVM. Therefore, in our experiment, ELM is applied to classify the feature vectors of pixels. Unlike the commonly used

percentage-based method, a small fixed number of each class is adopted to obtain training samples in our experiment. In the experiment, 3, 5, 10, 15, and 20 training samples for each class are applied for training ELM model, and the rest of samples are used for testing.

In this article, overall accuracy (OA), average accuracy (AA), and kappa coefficient [κ] are used to evaluate the classification result. Quantitatively, the greater the values of OA, AA, and kappa coefficient are, the better the classification result is.

In order to avoid the accidental phenomenon, the classification experiments of each feature descriptor are repeated 10 times, and a fixed number of training samples are randomly selected at each times. In the section named statistical table of classification results, classification accuracy mean and variance of each feature descriptor are shown in the experimental statistical table.

C. Experimental Result and Analysis

In this section, for the purpose of verifying the effectiveness of our proposed MDLBP descriptors, the classification results of different feature descriptors on two HSI data sets are analyzed intuitively and quantitatively.

1) Influence of the Parameter k of kB-SCN: As mentioned above, our proposed MDLBP descriptor is obtained by calculating the geometry difference between the multidimensional description sets of kB-SCNs. To explore the impact of parameter k on the classification result of MDLBP, we perform HSI pixel classification on four different MDLBP descriptors, including MDLBP-length, MDLBP-angle, MDLBP-projection, and MDLBP-fusion. As Fig. 5 shows, when k

TABLE I

CLASSIFICATION ACCURACY (%) USING SPECTRAL, 2-D-ULBP, VLBP, LBP-TOP, MDLBP-LENGTH, MDLBP-ANGLE, MDLBP-PROJECTION, AND MDLBP-FUSION ON THE TESTING SET OF INDIAN PINE DATA SET, WITH THREE LABELED SAMPLES PER CLASS AS TRAINING SET

Class	Spectral		2D-ULBP		VLBP		LBP-TOP		MDLBP-Length		MDLBP-Angle		MDLBP-Projection		MDLBP-Fusion	
	Mean	Var	Mean	Var	Mean	Var	Mean	Var	Mean	Var	Mean	Var	Mean	Var	Mean	Var
1	59.53	2.73	99.53	0.02	97.91	0.09	98.37	0.09	99.77	0.01	99.07	0.09	98.14	0.16	99.77	0.01
2	28.70	0.39	40.96	0.84	37.30	2.72	46.22	1.48	46.67	0.39	53.98	0.24	47.97	1.86	52.94	0.57
3	27.17	1.19	30.24	0.86	30.16	0.55	35.36	1.16	37.28	1.72	39.95	1.20	40.07	0.62	35.38	0.94
4	34.70	2.85	84.19	0.91	80.94	1.23	89.08	0.49	91.02	0.46	92.18	0.29	87.61	0.62	82.90	0.54
5	48.62	1.14	42.56	1.39	51.58	2.03	58.31	1.34	59.06	2.41	64.77	0.58	59.92	0.66	52.19	2.41
6	66.97	1.08	60.14	1.58	74.70	0.69	72.64	2.06	66.11	2.75	70.03	0.66	72.79	1.66	80.33	0.29
7	84.40	0.73	100.00	0.00	100.00	0.00	100.00	0.00	100.00	0.00	99.60	0.02	99.20	0.03	100.00	0.00
8	44.82	0.31	82.67	1.51	90.29	0.32	89.39	1.51	87.56	1.13	90.27	1.53	97.03	0.17	95.30	0.11
9	67.06	5.70	100.00	0.00	100.00	0.00	100.00	0.00	98.82	0.14	100.00	0.00	100.00	0.00	98.82	0.14
10	28.05	1.13	51.48	1.60	52.38	3.09	58.29	2.06	59.84	1.51	54.91	1.08	59.09	1.62	64.02	0.96
11	35.40	1.41	27.96	0.42	47.89	1.15	53.53	3.52	53.83	0.75	53.89	0.93	51.41	1.58	57.56	0.99
12	18.52	0.53	33.63	0.40	41.52	0.97	40.15	1.65	46.36	1.26	48.56	0.78	45.98	1.18	45.56	2.10
13	87.57	1.38	93.22	0.60	94.26	1.08	95.05	0.66	94.31	0.35	91.83	0.43	97.48	0.22	98.02	0.08
14	53.57	2.18	59.07	0.88	79.46	0.90	82.12	0.94	88.21	0.65	85.61	0.40	84.70	0.99	88.24	0.69
15	31.59	0.86	49.24	1.04	54.88	1.55	64.31	2.89	65.33	2.98	65.25	2.69	65.25	0.46	65.98	1.91
16	83.33	0.23	98.89	0.04	97.00	0.19	96.56	0.59	96.33	0.18	93.11	1.39	94.56	1.27	96.11	0.24
OA	39.40	0.18	46.51	0.07	55.80	0.08	60.31	0.29	61.42	0.14	62.62	0.12	61.63	0.21	64.35	0.06
AA	50.04	0.08	65.86	0.03	70.64	0.06	73.71	0.05	74.41	0.04	75.19	0.05	75.07	0.04	75.82	0.06
κ	32.70	0.17	41.61	0.08	51.19	0.09	56.06	0.32	57.18	0.16	58.47	0.13	57.64	0.22	60.36	0.08

TABLE II

CLASSIFICATION ACCURACY (%) USING SPECTRAL, 2-D-ULBP, VLBP, LBP-TOP, MDLBP-LENGTH, MDLBP-ANGLE, MDLBP-PROJECTION, AND MDLBP-FUSION ON THE TESTING SET OF SALINAS SCENE DATA SET, WITH THREE LABELED SAMPLES PER CLASS AS TRAINING SET

Class	Spectral		2D-ULBP		VLBP		LBP-TOP		MDLBP-Length		MDLBP-Angle		MDLBP-Projection		MDLBP-Fusion	
	Mean	Var	Mean	Var	Mean	Var	Mean	Var	Mean	Var	Mean	Var	Mean	Var	Mean	Var
1	98.77	0.00	73.87	1.21	86.77	0.52	91.51	0.21	93.26	0.19	92.96	0.12	91.83	0.16	92.19	0.17
2	92.06	0.64	61.10	1.17	90.96	1.47	98.48	0.04	96.07	0.52	95.22	0.15	95.48	0.99	98.10	0.23
3	27.48	1.41	73.05	1.80	83.75	1.47	90.54	0.50	89.34	2.01	92.65	0.44	89.48	1.41	94.94	1.07
4	99.49	0.00	95.79	0.12	95.21	0.08	97.29	0.01	94.34	0.13	94.16	0.24	95.82	0.13	95.05	0.15
5	98.67	0.00	70.06	1.49	88.99	0.31	94.97	0.09	94.83	0.13	93.06	0.19	95.60	0.02	95.26	0.02
6	98.68	0.01	66.30	0.91	95.27	0.05	94.12	0.18	96.06	0.05	89.41	0.20	96.10	0.09	95.33	0.09
7	99.59	0.00	63.25	3.16	86.46	1.03	90.43	0.24	92.86	0.23	90.28	0.36	92.88	0.50	94.89	0.09
8	51.49	8.78	44.24	2.11	62.87	2.34	67.83	3.11	72.65	2.20	76.82	0.88	61.31	2.77	69.26	1.48
9	97.59	0.09	52.19	1.61	93.58	0.32	97.02	0.07	98.60	0.00	97.92	0.03	99.30	0.00	99.01	0.00
10	76.91	0.15	48.05	0.92	77.25	1.10	82.01	1.23	80.54	0.86	81.56	0.86	84.62	0.51	84.09	0.35
11	91.15	0.05	69.25	4.06	92.71	0.06	94.17	0.05	94.35	0.01	93.11	0.05	94.74	0.07	94.60	0.05
12	88.05	0.89	58.28	3.05	80.91	0.38	86.58	0.72	87.44	0.73	86.75	0.26	88.59	0.33	88.99	0.33
13	98.28	0.01	75.64	0.74	87.80	0.24	83.38	2.00	89.26	0.16	84.52	0.80	91.93	0.33	91.91	0.10
14	91.88	0.14	78.85	0.74	76.50	3.85	81.98	1.34	84.27	4.00	83.85	0.47	85.90	0.44	85.10	0.90
15	60.47	5.82	41.60	1.80	76.67	0.72	81.53	1.55	75.72	0.96	80.18	0.99	80.97	1.67	84.01	0.67
16	91.54	0.20	55.72	1.32	80.12	1.01	87.47	0.34	84.18	1.64	79.02	1.01	82.30	0.87	79.92	0.63
OA	78.40	0.12	56.40	0.09	81.25	0.10	85.59	0.10	86.05	0.06	86.50	0.03	84.78	0.08	87.13	0.05
AA	85.13	0.02	64.20	0.07	84.74	0.03	88.71	0.04	88.99	0.03	88.22	0.01	89.18	0.04	90.17	0.03
κ	76.06	0.14	52.16	0.09	79.30	0.12	84.08	0.13	84.54	0.08	85.01	0.04	83.16	0.09	85.75	0.06

TABLE III
CLASSIFICATION ACCURACY (%) USING 3-D-DWT, 3-D-SIFT, 3-D-GABOR, TGSIFT, 3-D-DL, 3-D-CNN, M3D-DCNN, AND MDLBP-FUSION ON THE TESTING SET OF INDIAN PINE DATA SET, WITH THREE LABELED SAMPLES PER CLASS AS TRAINING SET

Class	3D-DWT		3D-SIFT		3D-Gabor		TGSIFT		3D-DL		3D-CNN		M3D-DCNN		MDLBP-Fusion	
	Mean	Var	Mean	Var	Mean	Var	Mean	Var	Mean	Var	Mean	Var	Mean	Var	Mean	Var
1	81.86	8.55	97.91	0.34	80.47	1.72	89.07	9.84	4.47	0.39	3.08	0.32	30.69	3.83	99.77	0.01
2	33.27	1.28	34.74	0.59	32.96	1.14	41.33	1.83	15.80	2.51	10.40	2.59	23.59	1.32	52.94	0.57
3	19.01	0.46	33.26	1.74	31.79	1.20	43.47	1.70	6.34	0.84	7.55	1.00	13.84	0.32	35.38	0.94
4	59.06	3.23	65.47	7.63	41.84	2.14	93.80	0.51	7.93	0.95	5.21	0.52	19.92	0.19	82.90	0.54
5	49.87	4.03	46.88	1.39	42.40	3.83	54.89	0.59	14.03	1.62	6.71	1.20	20.73	2.11	52.19	2.41
6	75.46	2.43	55.53	2.82	56.77	0.94	60.99	4.15	26.72	7.60	11.56	6.45	55.94	3.41	80.33	0.29
7	99.60	0.02	100.00	0.00	100.00	0.00	100.00	0.00	3.23	0.14	3.58	0.51	9.46	0.07	100.00	0.00
8	65.11	1.87	79.37	1.10	95.33	0.10	99.35	0.01	22.17	7.63	16.72	11.35	68.98	0.85	95.30	0.11
9	98.82	0.14	99.41	0.03	98.82	0.06	100.00	0.00	9.03	2.43	2.43	0.18	20.67	0.25	98.82	0.14
10	46.10	3.29	36.56	3.83	34.79	6.49	57.67	0.97	10.12	1.47	6.77	1.18	28.50	1.27	64.02	0.96
11	46.07	2.53	37.78	1.38	48.12	2.38	50.67	1.08	11.57	4.11	5.27	1.30	36.00	3.84	57.56	0.99
12	26.58	1.17	31.02	1.57	22.61	0.37	47.44	1.18	6.01	0.47	3.28	0.54	15.67	0.26	45.56	2.10
13	87.77	0.71	92.23	0.11	93.71	0.23	94.06	0.91	12.66	2.55	10.24	4.20	57.77	1.23	98.02	0.08
14	89.56	0.26	85.13	1.42	78.42	0.89	78.49	0.92	39.76	12.80	37.22	7.46	68.56	2.92	88.24	0.69
15	45.51	2.39	66.34	4.64	55.46	1.97	85.56	1.43	4.41	0.86	0.00	0.00	12.94	0.72	65.98	1.91
16	96.00	0.36	96.44	0.42	99.89	0.00	87.56	9.94	68.53	10.87	18.01	8.32	49.45	6.01	96.11	0.24
OA	51.42	0.14	49.78	0.06	50.07	0.10	59.75	0.13	23.12	0.44	18.18	0.67	37.84	0.20	64.35	0.06
AA	63.73	0.12	66.13	0.07	63.34	0.05	74.03	0.14	16.42	0.21	9.25	1.07	33.30	0.13	75.82	0.06
κ	45.31	0.16	44.36	0.07	44.02	0.13	55.65	0.14	16.10	0.35	10.19	0.76	30.89	0.17	60.36	0.08

increases, the OA of the four MDLBP descriptors shows a trend of increasing first and then decreasing. The reason for the decrease of classification accuracy is the data redundancy caused by the high dimension of kB-SCN. When k is 4, the classification accuracies of the four MDLBP descriptors are the best. In the following experiments, the parameter k will be set to 4, and the parameters of all kinds of LBP descriptors will be set uniformly. In our experiment, the radius of neighborhood, the number of neighborhood sampling points, and the neighbor-hood size are empirically set to 3, 8, and $8 \times 8 \times 8$, respectively.

2) *Influence of the Training Sample Size*: In order to verify the effectiveness of the MDLBP algorithm in the scenery of a small number of training samples, we take 3, 5, 10, 15, and 20 labeled samples for each class when training. Two groups of experiments were conducted on the two HSI data sets. Therefore, the curve change of the classification results of eight descriptors is obtained, as shown in Figs. 6 and 7. As the number of training samples increases, the OA and Kappa coefficient of each descriptor increase. Among them, the OA of our proposed MDLBP-Fusion is always the best in terms of different training sample sizes. Besides, the performance of MDLBP descriptor based on the single-dimensional description is also better than the 2-D-LBP and 3-D-LBP descriptors. When the number of training samples is less, the gap between the classification accuracy of various descriptors increases. When the number of training samples

is 3, the gap reaches the maximum, and the OA of our proposed MDLBP-Fusion descriptor is increased by 1.54% when comparing with 3-D-LBP descriptor. In summary, our proposed MDLBP descriptor shows better performance in the scenery of a small number of labeled samples for the classification of HSI.

3) *Classification Maps of Different Algorithms*: Our HSI classification experiment is first conducted on the Indian Pine data set, Fig. 8 shows the classification maps of eight feature descriptors when the number of training samples is 3. Comparing the label maps of ground truth with that of the spectral feature, we can know that using only the spectral information is not enough to describe the HSI feature information. The classification result is greatly improved after the application of LBP algorithm. Among them, the performance of the 3-D LBP-TOP is better than that of 2-D-ULBP and VLBP. Moreover, the four MDLBP descriptors proposed in this article all show excellent performance in the case of small labeled samples, and the labeled map of MDLBP-fusion descriptor is the closest map to the ground truth.

Fig. 9 shows the classification maps of the eight feature descriptors on the Salinas scene data set when the number of training samples for each class is 3. From Fig. 9, it can be seen that the classification result of the spectral feature is significantly better than the 2-D-ULBP descriptor, which indicates that HSI pixels of the Salinas scene data set have excellent spectral discrimination. VLBP and LBPTOP which

TABLE IV
CLASSIFICATION ACCURACY (%) USING 3-D-DWT, 3-D-SIFT, 3-D-GABOR, TGSIFT, 3-D-DL, 3-D-CNN, M3D-DCNN, AND MDLBP-FUSION ON THE TESTING SET OF SALINAS SCENE DATA SET, WITH THREE LABELED SAMPLES PER CLASS AS TRAINING SET

Class	3D-DWT		3D-SIFT		3D-Gabor		TGSIFT		3D-DL		3D-CNN		M3D-DCNN		MDLBP-Fusion	
	Mean	Var	Mean	Var	Mean	Var	Mean	Var	Mean	Var	Mean	Var	Mean	Var	Mean	Var
1	98.35	0.00	94.64	0.12	92.67	0.06	78.30	2.05	15.14	3.62	53.14	14.98	52.50	14.58	92.19	0.17
2	86.54	0.73	88.43	1.85	83.34	0.52	82.66	1.10	15.43	4.35	45.35	17.11	60.97	10.38	98.10	0.23
3	23.92	2.95	75.45	2.24	16.92	1.53	89.76	0.36	2.52	0.29	43.68	13.19	46.50	8.81	94.94	1.07
4	97.47	0.02	90.69	1.67	94.24	0.11	81.43	1.10	53.80	13.70	58.79	19.50	88.34	2.98	95.05	0.15
5	96.09	0.18	87.07	2.92	76.96	1.00	67.73	1.45	18.46	1.56	47.99	16.03	77.25	6.83	95.26	0.02
6	96.93	0.01	99.29	0.00	91.38	0.02	70.34	1.97	41.44	15.59	63.05	18.83	96.77	0.01	95.33	0.09
7	95.81	0.03	93.65	0.27	86.08	0.45	75.53	1.31	15.26	5.45	54.00	19.99	62.39	11.67	94.89	0.09
8	73.35	1.41	75.89	1.44	64.25	2.46	50.92	2.55	35.57	9.80	28.93	8.96	52.47	4.95	69.26	1.48
9	96.15	0.00	93.10	0.16	93.67	0.49	65.63	0.67	20.49	6.37	47.59	20.39	52.50	16.11	99.01	0.00
10	80.76	0.17	69.03	2.09	79.32	0.93	61.48	3.10	3.74	0.39	40.58	12.65	34.50	3.72	84.09	0.35
11	93.74	0.31	94.68	1.32	85.28	4.49	80.55	1.34	3.57	0.32	34.27	7.65	24.84	3.39	94.60	0.05
12	95.88	0.32	88.72	0.36	97.93	0.08	68.60	1.58	12.77	1.79	52.68	19.33	41.53	12.59	88.99	0.33
13	92.70	0.51	94.29	0.43	95.25	0.39	51.96	1.31	19.53	7.20	51.00	14.52	82.88	2.93	91.91	0.10
14	78.98	4.59	86.31	1.67	85.03	0.63	71.78	1.32	20.52	8.21	43.48	18.49	78.25	6.17	85.10	0.90
15	53.09	3.03	67.64	6.27	63.55	6.15	56.97	4.43	32.73	6.68	36.05	6.17	39.25	4.97	84.01	0.67
16	85.80	0.25	77.12	2.98	70.89	0.31	95.38	0.27	27.07	7.35	39.69	13.76	61.72	3.85	79.92	0.63
OA	80.73	0.02	83.08	0.10	76.68	0.08	66.47	0.09	32.34	0.88	45.83	8.89	60.00	1.03	87.13	0.05
AA	84.10	0.02	86.00	0.08	79.80	0.09	71.81	0.05	21.13	0.48	46.27	11.79	59.54	1.91	90.17	0.03
κ	78.57	0.02	81.17	0.13	74.16	0.10	63.32	0.10	26.52	0.73	42.46	9.35	56.14	1.14	85.75	0.06

combine the spatial and spectral information show excellent performance compared with 2-D-ULBP. Since our proposed MDLBP descriptor can fully describe the spatial–spectral feature of HSI, it is more robust than the spectral features and traditional LBP descriptors.

4) *Statistical Table of Classification Results:* As observed from Table I, the classification accuracies of feature descriptors using the LBP algorithm are significantly higher than that of spectral feature descriptors, while the classification accuracies of 3-D LBP descriptors are significantly better than that of traditional 2-D LBP descriptors. Moreover, compared with 3-D-LBP descriptor, three kinds of MDLBP descriptor based on single-dimensional description is at least increased by 1.11%, while the OA of MDLBP-fusion descriptor is 64.35% which is 4.04% higher than the LBP-TOP descriptor. To sum up, 3-D-LBP descriptor developed for video processing cannot fully utilize spatial and spectral information, further verifying the effectiveness of our proposed MDLBP algorithm.

As shown in Table II, in the Salinas scene data set, the OA of the spectral curve features is 78.40%, which is 22% higher than that of 2-D-ULBP descriptor, showing its excellent classification performance for vegetable crops. In contrast, 2-D-ULBP algorithms which only extract the spatial information will destroy the correlation between spectral bands, resulting in poor classification results. Our proposed MDLBP-Fusion descriptor which fully utilizes the spatial–spectral information achieves the highest accuracy. Therefore, it further demonstrates the strong robustness of our proposed MDLBP descriptor.

In addition to the comparison with LBP-based algorithms, seven representative spatial–spectral feature extraction algorithms are also used for comparison to prove the efficiency of our proposed MDLBP. As shown in Table III, most of the accuracies achieved by MDLBP-fusion are better than those yielded by other 3-D handcraft feature descriptors. Besides, the results obtained by 3-D handcraft feature descriptors are better than that of the deep learning-based algorithms, which demonstrates the inapplicability of deep learning-based algorithms in a small labeled sample problem.

From Table IV, it can be seen that the OA of MDLBP-Fusion descriptor is 87.13%, while the OA of 3-D-DWT, 3-D-SIFT, 3-D-Gabor, and TGSIFT algorithms are 80.73%, 83.08%, 76.68%, and 66.47%, respectively. Moreover, the deep learning-based algorithms can reach only 60.00%, which further shows that the MDLBP algorithm is an excellent solution to the small sample classification problem of HSI pixels.

In summary, the performance of our MDLBP algorithm in HSI pixel classification is better than that of LBP-based and other representative spatial–spectral feature extraction algorithms, especially when the training sample size is small.

VI. CONCLUSION

In this article, based on Clifford algebra, a novel MDLBP algorithm for HSI is proposed. The MDLBP algorithm calculates the geometric relationship between the local geometry of HSI using different geometric operation methods, and obtains a multidimensional description set that can effectively represent the feature of the local spatial–spectral informa-

tion. According to the traditional LBP algorithm, the local binary coding for the spatial-spectral information of HSI is implemented by calculating the geometric difference between the multidimensional description sets. Moreover, our proposed MDLBP algorithm has the advantage of expandability and interpretability. Experimental results on two public HSI data sets show that our proposed MDLBP algorithm can achieve higher accuracy than the representative spatial-spectral feature and existing LBP algorithms, especially when the training sample size is small. In summary, we not only present an excellent LBP algorithm for HSI classification, but also provide a new idea which can provide a strict mathematical deduction for the representation of local features of images.

REFERENCES

- [1] S. Ortega, H. Fabelo, R. Camacho, M. de la Luz Plaza, G. M. Callicó, and R. Sarmiento, "Detecting brain tumor in pathological slides using hyperspectral imaging," *Biomed. Opt. Exp.*, vol. 9, no. 2, pp. 818–831, Feb. 2018.
- [2] B. S. Sorg, B. J. Moeller, O. Donovan, Y. Cao, and M. W. Dewhurst, "Hyperspectral imaging of hemoglobin saturation in tumor microvasculature and tumor hypoxia development," *J. Biomed. Opt.*, vol. 10, no. 4, 2005, Art. no. 044004.
- [3] L. Ravikanth, D. S. Jayas, N. D. G. White, P. G. Fields, and D.-W. Sun, "Extraction of spectral information from hyperspectral data and application of hyperspectral imaging for food and agricultural products," *Food Bioprocess Technol.*, vol. 10, no. 1, pp. 1–33, Jan. 2017.
- [4] M. Z. M. Jafri and S. C. Tan, "Feature selection from hyperspectral imaging for guava fruit defects detection," *Digit. Opt. Technol., Int. Soc. Opt. Photon.*, vol. 10335, Jun. 2017, Art. no. 103351E.
- [5] M. V. Kumar and K. Yarrakula, "Comparison of efficient techniques of hyper-spectral image preprocessing for mineralogy and vegetation studies," *Indian J. Geo-Marine Sci.*, vol. 46, pp. 1008–1021, May 2017.
- [6] Z. Aslett, J. V. Taranik, and D. N. Riley, "Mapping rock forming minerals at Boundary Canyon, Death Valley National Park, California, using aerial SEBASS thermal infrared hyperspectral image data," *Int. J. Appl. Earth Observ. Geoinf.*, vol. 64, pp. 326–339, Feb. 2018.
- [7] Y. Sun, W. Lei, and X. Ren, "The research status and application of hyperspectral image target detection," in *Proc. Sel. Papers Chin. Soc. Opt. Eng. Conf., Int. Soc. Opt. Photon.*, vol. 10255, Nov. 2016, Art. no. 102554T.
- [8] M. Uzair, A. Mahmood, and A. Mian, "Hyperspectral face recognition with spatiotemporal information fusion and PLS regression," *IEEE Trans. Image Process.*, vol. 24, no. 3, pp. 1127–1137, Mar. 2015.
- [9] A. Ghasemzadeh and H. Demirel, "3D discrete wavelet transform-based feature extraction for hyperspectral face recognition," *IET Biometrics*, vol. 7, no. 1, pp. 49–55, Jan. 2018.
- [10] T. Ojala, M. Pietikäinen, and T. Maenpää, "Multiresolution gray-scale and rotation invariant texture classification with local binary patterns," *IEEE Trans. Pattern Anal. Mach. Intell.*, vol. 24, no. 7, pp. 971–987, Jul. 2002.
- [11] T. Ahonen, A. Hadid, and M. Pietikäinen, "Face recognition with local binary patterns," in *Proc. Eur. Conf. Comput. Vis.* Berlin, Germany: Springer, 2004, pp. 469–481.
- [12] G. Zhao, T. Ahonen, J. Matas, and M. Pietikäinen, "Rotation-invariant image and video description with local binary pattern features," *IEEE Trans. Image Process.*, vol. 21, no. 4, pp. 1465–1477, Apr. 2012.
- [13] W. Chuan-Xu and L. Zuo-Yong, "A new face tracking algorithm based on local binary pattern and skin color information," in *Proc. Int. Symp. Comput. Sci. Comput. Technol. (ISCSCT)*, vol. 2, 2008, pp. 657–660.
- [14] D. K. Iakovidis, E. G. Keramidas, and D. Maroulis, "Fuzzy local binary patterns for ultrasound texture characterization," in *Proc. Int. Conf. Image Anal. Recognit.* Berlin, Germany: Springer, 2008, pp. 750–759.
- [15] L. Paulhac, P. Makris, and J. Y. Ramel, "Comparison between 2D and 3D local binary pattern methods for characterisation of three-dimensional textures," in *Proc. Int. Conf. Image Anal. Recognit.* Berlin, Germany: Springer, 2008, pp. 670–679.
- [16] C. Song, F. Yang, and P. Li, "Rotation invariant texture measured by local binary pattern for remote sensing image classification," in *Proc. 2nd Int. Workshop Educ. Technol. Comput. Sci.*, 2010, pp. 3–6.
- [17] W. Li, C. Chen, H. Su, and Q. Du, "Local binary patterns and extreme learning machine for hyperspectral imagery classification," *IEEE Trans. Geosci. Remote Sens.*, vol. 53, no. 7, pp. 3681–3693, Jul. 2015.
- [18] S. Jia, J. Hu, J. Zhu, X. Jia, and Q. Li, "Three-dimensional local binary patterns for hyperspectral imagery classification," *IEEE Trans. Geosci. Remote Sens.*, vol. 55, no. 4, pp. 2399–2413, Apr. 2017.
- [19] G. Zhao and M. Pietikäinen, "Dynamic texture recognition using local binary patterns with an application to facial expressions," *IEEE Trans. Pattern Anal. Mach. Intell.*, vol. 29, no. 6, pp. 915–928, Jun. 2007.
- [20] B. Q. Song and P. J. Li, "The application of extended lbp texture in high resolution remote sensing image classification," *Remote Sens. Land Resour.*, vol. 25, no. 4, pp. 40–45, 2010.
- [21] Z. Ye, J. E. Fowler, and L. Bai, "Spatial-spectral hyperspectral classification using local binary patterns and Markov random fields," *J. Appl. Remote Sens.*, vol. 11, no. 3, Jul. 2017, Art. no. 035002.
- [22] P. Sidike, C. Chen, V. Asari, Y. Xu, and W. Li, "Classification of hyperspectral image using multiscale spatial texture features," in *Proc. 8th Workshop Hyperspectral Image Signal Process., Evol. Remote Sens. (WHISPERS)*, Aug. 2016, pp. 1–4.
- [23] Y. Li *et al.*, "A novel local binary pattern descriptor based on spectral vector for hyperspectral image," in *Proc. IET 7th Int. Conf. Wireless, Mobile Multi-Media*, Nov. 2017, pp. 108–113.
- [24] Y. Li, H. Tang, L. Fan, and W. Luo, "TSSLBP: Tensor-based spatial-spectral local binary pattern," *J. Appl. Remote Sens.*, vol. 14, no. 3, Jan. 2020, Art. no. 032606.
- [25] H. Yang, Y. Yang, F. Gao, and J. Dong, "Hyperspectral image classification based on local binary patterns and PCANet," in *Proc. 9th Int. Conf. Graphic Image Process. (ICGIP)*, Apr. 2018, Art. no. 106152X.
- [26] X. Wei, X. Yu, B. Liu, and L. Zhi, "Convolutional neural networks and local binary patterns for hyperspectral image classification," *Eur. J. Remote Sens.*, vol. 52, no. 1, pp. 448–462, Jan. 2019.
- [27] X. Cao, L. Xu, D. Meng, Q. Zhao, and Z. Xu, "Integration of 3-dimensional discrete wavelet transform and Markov random field for hyperspectral image classification," *Neurocomputing*, vol. 226, pp. 90–100, Feb. 2017.
- [28] L. He, J. Li, A. Plaza, and Y. Li, "Discriminative low-rank Gabor filtering for spectral-spatial hyperspectral image classification," *IEEE Trans. Geosci. Remote Sensing*, vol. 55, no. 3, pp. 1381–1395, Dec. 2017.
- [29] P. Scovanner, "A 3-dimensional sift descriptor and its application to action recognition," in *Proc. ACM Multimedia*, 2007, pp. 357–360.
- [30] Y. Li and W. Shi, "A new framework of hyperspectral image classification based on spatial spectral interest point," in *Proc. IEEE 13th Int. Conf. Signal Process. (ICSP)*, Nov. 2016, pp. 733–736.
- [31] Y. Li, L. Fan, and W. Xie, "TGSIFT: Robust SIFT descriptor based on tensor gradient for hyperspectral images," *Chin. J. Electron.*, vol. 29, no. 5, pp. 916–925, Sep. 2020.
- [32] M. M. Dalla, A. Villa, J. A. Benediktsson, J. Chanussot, and L. Bruzzone, "Classification of hyperspectral images by using extended morphological attribute profiles and independent component analysis," *IEEE Geosci. Remote Sens. Lett.*, vol. 8, no. 3, pp. 542–546, Dec. 2011.
- [33] Y. Li, H. Zhang, and Q. Shen, "Spectral-spatial classification of hyperspectral imagery with 3D convolutional neural network," *Remote Sens.*, vol. 9, no. 1, p. 67, Jan. 2017.
- [34] A. Ben Hamida, A. Benoit, P. Lambert, and C. Ben Amar, "3-D deep learning approach for remote sensing image classification," *IEEE Trans. Geosci. Remote Sens.*, vol. 56, no. 8, pp. 4420–4434, Aug. 2018.
- [35] Y. Chen, H. Jiang, C. Li, X. Jia, and P. Ghamisi, "Deep feature extraction and classification of hyperspectral images based on convolutional neural networks," *IEEE Trans. Geosci. Remote Sens.*, vol. 54, no. 10, pp. 6232–6251, Oct. 2016.
- [36] M. He, B. Li, and H. Chen, "Multi-scale 3D deep convolutional neural network for hyperspectral image classification," in *Proc. IEEE Int. Conf. Image Process. (ICIP)*, Sep. 2017, pp. 3904–3908.
- [37] S. Buchholz and G. Sommer, "On clifford neurons and clifford multi-layer perceptrons," *Neural Netw.*, vol. 21, no. 7, pp. 925–935, Sep. 2008.
- [38] A. Chapman and U. Vishne, "Clifford algebras of binary homogeneous forms," *J. Algebra*, vol. 366, pp. 94–111, Sep. 2012.
- [39] D. Hestenes and G. Sobczyk, *Clifford Algebra to Geometric Calculus: A Unified Language for Mathematics and Physics*. Springer, 2012.
- [40] H. Li, D. Hestenes, and A. Rockwood, "Generalized homogeneous coordinates for computational geometry," in *Geometric Computing with Clifford Algebras*. Berlin, Germany: Springer, 2001, pp. 27–59.
- [41] R. Penrose and W. Rindler, *Spinors and Space-Time: Spinor and Twistor Methods in Space-Time Geometry*, vol. 2. Cambridge, U.K.: Cambridge Univ. Press, 1986.

- [42] G. Sommer, *Geometric Computing With Clifford Algebras: Theoretical Foundations and Applications in Computer Vision and Robotics*. Springer, 2013.
- [43] J. Byrnes and G. Ostheimer, *Computational Noncommutative Algebra and Applications: Proceedings of the NATO Advanced Study Institute, on Computational Noncommutative Algebra and Applications*, Il Ciocco, Italy: Springer, Jul. 2006, pp. 6–19.
- [44] W. Xie, W. Cao, and S. Meng, “Coverage analysis for sensor networks based on Clifford algebra,” *Sci. China Ser. F, Inf. Sci.*, vol. 51, no. 5, pp. 460–475, May 2008.
- [45] F. Brackx, N. De Schepper, and F. Sommen, “The clifford-Fourier transform,” *J. Fourier Anal. Appl.*, vol. 11, no. 6, pp. 669–681, Dec. 2005.
- [46] L. I. Yan-shan, “A digital image watermarking algorithm based on Clifford algebra,” *Acta Electronica Sinica*, vol. 5, pp. 852–855, May 2008.
- [47] M. Schlemmer, “Fourier transformation and filter design for Clifford convolution,” M.S. thesis, Univ. Kaiserslautern, Kaiserslautern, Germany, 2004. [Online]. Available: <http://www-hagen.informatik.uni-kl.de/~schlemmer>
- [48] V. Labunets, “Clifford algebras as unified language for image processing and pattern recognition,” in *Computational Noncommutative Algebra and Applications*. Dordrecht, The Netherlands: Springer, 2004, pp. 197–225.
- [49] S. Wold, K. Esbensen, and P. Geladi, “Principal component analysis,” *Chemometrics Intell. Lab. Syst.*, vol. 2, nos. 1–3, pp. 37–52, 1987.
- [50] G.-B. Huang, Q.-Y. Zhu, and C.-K. Siew, “Extreme learning machine: Theory and applications,” *Neurocomputing*, vol. 70, nos. 1–3, pp. 489–501, Dec. 2006.
- [51] R. G. Congalton, “A review of assessing the accuracy of classifications of remotely sensed data,” *Remote Sens. Environ.*, vol. 37, no. 1, pp. 35–46, Jul. 1991.



Yanshan Li received the M.Sc. degree from the Zhejiang University of Technology, Hangzhou, China, in 2005, and the Ph.D. degree from the South China University of Technology, Guangzhou, China, in 2015.

He is an Associate Professor with the ATR National Key Laboratory of Defense Technology, Shenzhen University, Shenzhen, China. His research interests cover computer vision, machine learning, and image analysis.



Haojin Tang received the B.E. degree in information and engineering from Shenzhen University, Shenzhen, China, in 2018, where he is pursuing the Ph.D. degree in intelligent information processing with the College of Electronic and Information Engineering.

His research interests include hyperspectral image processing, computer vision, and few-shot learning.



Weixin Xie received the B.E. degree from Xidian University, Xi'an, China, in 1965.

He joined Xidian University, as a Faculty Member, in 1965. From 1981 to 1983, he was a Visiting Scholar with the University of Pennsylvania, Philadelphia, PA, USA, where he joined as a Visiting Professor in 1989. He is with the School of Information Engineering, Shenzhen University, Shenzhen, China. His research interests include intelligent information processing, fuzzy information processing, image processing, and pattern recognition.



Wenhan Luo received the B.E. degree from the Huazhong University of Science and Technology, Wuhan, China, in 2009, the M.E. degree from the Institute of Automation, Chinese Academy of Sciences, Beijing, China, in 2012, and the Ph.D. degree from the Imperial College London, London, U.K., in 2016.

His research interests include several topics in computer vision and machine learning, such as motion analysis (especially object tracking), image/video quality restoration, object detection and recognition, and reinforcement learning.